

HIGH-RESOLUTION PROBABILISTIC DATA-DRIVEN WEATHER MODELING WITH A STRETCHED-GRID

Even Marius Nordhagen ^{a†*}Håvard Homleid Haugen ^{a†}Aram Farhad Shafiq Salihi ^aMagnus Sikora Ingstad ^aThomas Nils Nipen ^aIvar Ambjørn Seierstad ^aInger-Lise Frogner ^aMariana Clare ^cSimon Lang ^bMatthew Chantry ^bPeter Dueben ^cJørn Kristiansen ^a

ABSTRACT

We present a probabilistic data-driven weather model capable of providing an ensemble of high spatial resolution realizations of 87 variables at arbitrary forecast length and ensemble size. The model uses a stretched grid, dedicating 2.5 km resolution to a region of interest, and 31 km resolution elsewhere. Based on a stochastic encoder–decoder architecture, the model is trained using a loss function based on the Continuous Ranked Probability Score (CRPS) evaluated point-wise in real and spectral space. The spectral loss components is shown to be necessary to create fields that are spatially coherent.

The model is compared to high-resolution operational numerical weather prediction forecasts from the MetCoOp Ensemble Prediction System (MEPS), showing competitive forecasts when evaluated against observations from surface weather stations. The model produced fields that are more spatially coherent than mean squared error based models and CRPS based models without the spectral component in the loss.

Keywords: Weather Forecasts · Machine Learning · Probabilistic · Ensembles · Graph Neural Networks

1 Introduction

Data-driven models (DDMs) have recently been shown to perform equal to or better than conventional numerical weather prediction (NWP) systems across a range of variables, while consuming a fraction of the computational cost when generating forecasts. Many of these models, including FourCastNet [1], PanguWeather [2], FuXi [3], and the Artificial Intelligence Forecasting System (AIFS) [4], are deterministic neural network-based models trained with a mean squared error (MSE) loss function. However, MSE is affected by the double penalty problem [5, 6, 7]:

if a model predicts an event slightly displaced from its observed location, it is penalized once for the false prediction and again for the missed true event. To minimize MSE, models are therefore encouraged to smoothen less predictable events, particularly extremes.

Addressing this challenge requires a training objective that is not based purely on the MSE. One approach is to retain the deterministic framing, but modify the loss function to encourage sharper spatial fields [8, 7]. Another alternative is to adopt probabilistic models that explicitly represent forecast uncertainty, which is also essential to predict extreme weather events. In data-driven weather prediction, these have predominantly relied on proper score-based and diffusion-based methods.

Proper Score-based approaches [9, 10, 11, 12, 13] directly optimize proper scoring rules such as Continuous Ranked Probability Score (CRPS) or the energy score, encourag-

^aNorwegian Meteorological Institute, Oslo, Norway

^bECMWF, Reading, UK

^cECMWF, Bonn, Germany

[†]Equal contribution

*Corresponding author: even.nordhagen@gmail.com

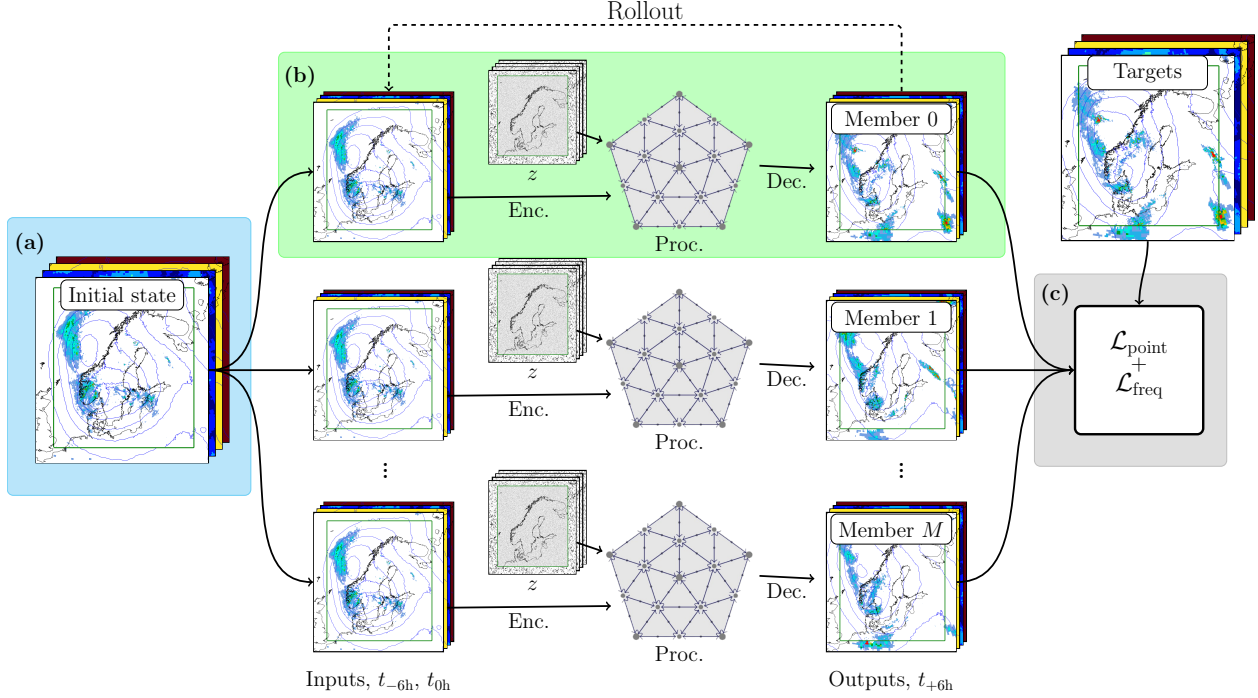


Figure 1: Schematic diagram of the ensemble training. (a) The preceding (t_{-6h}) and the current (t_{0h}) states from MEPS and ERA5 are used as inputs to the model. The inputs are replicated M times, where M is the number of ensemble members during training. (b) The model has an encoder-processor-decoder architecture, where noise (z) is injected into the latent space for stochasticity. (c) The predictions are evaluated against targets using a point-wise and spectral training objective.

ing reliable spread-skill relationship [14]. Stochasticity is incorporated into the model to generate distinct ensemble members. Because the architecture remains close to its deterministic counterpart and only the loss function is changed, score-based models have nearly identical computational cost per member as deterministic models.

Diffusion-based models [15, 16, 17] generally use similar architectures to deterministic networks, but are conditioned on varying noise levels. They are then trained to iteratively remove noise from input fields until sharp forecasts emerge. They are known for producing high-fidelity outputs, and because noise serves as their input, they are inherently stochastic and naturally suited for generating ensembles. However, each forecast typically requires 10–100 denoising steps, making diffusion models substantially more computationally expensive than deterministic and proper score-based approaches.

Global data-driven models typically operate at 0.25° resolution. Regional data-driven models can achieve significantly higher resolution, by focusing the model’s complexity on a small area. Regional models have recently been developed to exploit kilometer-scale forecasting, typically using either limited-area models (LAMs) [18, 17, 19], where a model receives boundary conditions from an external model, or stretched-grid models [20, 21], which are global models with higher resolution over an area of interest and

lower resolution elsewhere. For high-resolution modeling, the smoothing effect of the MSE loss is significant. As will be demonstrated, applying a CRPS approach directly to the high resolution case creates spatial fields that are spatially incoherent. We therefore further modify the CRPS approach by introducing a spectral term in the loss function that encourages correct spread at different spatial scales. The spectral term computes the CRPS of the Fourier coefficients obtained via the fast Fourier transform (FFT). We refer to this model as *Bris CRPS-FFT*. To our knowledge, *Bris CRPS-FFT* is the first ensemble DDM capable of realistically simulating weather at kilometer scale. We compare *Bris CRPS-FFT* to a model trained with point-wise CRPS only, and the deterministic MSE-based model in [20], here referred to as *Bris CRPS* and *Bris MSE*, respectively.

This paper is organized as follows: The model architecture and training approach is described in Sec. 2. Sec. 3 discusses the datasets used to train the model, and to perform inference. In Sec. 4, we verify the model against observations from weather stations, evaluating the characteristics of individual ensemble members as well as the probabilistic capabilities of the ensemble as a whole. Finally, conclusions are presented in Sec. 5.

Table 1: Model configurations, key properties and datasets used in the different training stages.

	Stage A	Stage B	Stage C
Global dataset	ERA5	ERA5	IFS
Global resolution	100 km	31 km	31 km
Global refinement	5	7	7
Regional dataset	—	—	MEPS
Regional resolution	—	—	2.5 km
Regional refinement	—	—	10
Number of grid nodes	40 k	540 k	1.3 M
Number of mesh nodes	10 k	164 k	284 k
Total number of edges	325 k	4.9 M	10.3 M

2 Methodology

2.1 Model architecture

The model uses graph neural networks (GNNs), which were first introduced to weather prediction by [22], and frequently used in other models [e.g. 4, 10]. GNNs have nodes, which are used to represent the atmosphere for a specific spatial location, and edges, which represent how nodes communicate information. This flexible architecture allows for arbitrary grid configurations and we follow the stretched-grid approach developed in [20], where regional analyses from the MetCoOp Ensemble Prediction System (MEPS) [23, 24] at 2.5 km resolution are used over the Nordic region, and ERA5 [25] is used at 31 km resolution elsewhere on the globe.

The two input datasets are passed through an *encoder* to a hidden mesh, which has a lower resolution than the input grid, but with a greater number of features. This hidden mesh has a variable resolution, where the resolution is proportional to the local resolution of the input grid. This latent representation is then passed through a *processor*, consisting of a number of message passing steps that allow the model to communicate information in space. Finally, the latent representation is passed through a *decoder* to the same grid as the input datasets. This process generates a 6-hour forecast, and the process can be repeated autoregressively to generate an arbitrary length forecast.

We have used the same settings as in [20], such as the embedding dimension (1024), number of attention heads (8) and number of message-passing steps (16), resulting in a similar number of trainable parameters (229 million). The graphs are also similar, with 7 refinement layers globally, 10 regionally, 12 encoder connections, and 3 decoder connections. This gives $N_{\text{mesh}} = 284,000$ hidden mesh nodes. In total, the model has 1.3 million input/output grid points.

The key novelty of our model is that it provides ensemble forecasts at kilometre scale. To represent stochastic processes in the atmosphere and to ensure inherently different ensemble members for an arbitrary ensemble size,

the model needs to be stochastic. This is done by injecting noise into the latent space through a multilayer perceptron (MLP) and conditional layernorms, following AIFS-CRPS [10] (Fig. 1). The MLP takes in Gaussian noise with dimensions $(4, N_{\text{mesh}})$, allowing the model to shape the noise according to the fields. The noise injector also takes information about the forecast step, allowing the model to incorporate different noise at different forecast lead times. During training, members are generated independently.

In order to generate skillful ensemble forecasts, the model is trained on Continuous Ranked Probability Score (CRPS) loss, which simultaneously optimizes the reliability and resolution. To quantify the spread, an ensemble size of 2 or more members is required during training. During inference an arbitrary number of members can be generated.

2.2 Training objective

The Continuous Ranked Probability Score (CRPS) loss depends only on the marginal distributions of the ensemble at each location and therefore is not scale aware [26]. Members can therefore appear to be spatially incoherent, when the model generates too much variability at a certain scale.

Different approaches have been proposed to address this issue. One strategy is to decompose the fields into different spatial scales and evaluate CRPS separately for each scale [26]. Another is to compute CRPS both in the physical and spectral space [12], which is the approach we are using here.

The training objective consists of a global and a regional component, similar to [20]. The global component, evaluated on the 31 km horizontal resolution grid, is the CRPS computed point-wise in space. The regional component, evaluated at 2.5 km horizontal resolution, combines a point-wise CRPS loss with a spectral CRPS loss.

Mathematically the training objective is expressed as:

$$\mathcal{L}(\{x\}, y) = \sum_v \sum_t w_v \left[\mathcal{L}_g(\{x_g\}, y_g) + \lambda_r \mathcal{L}_r(\{x_r\}, y_r) \right],$$

where \mathcal{L}_g and \mathcal{L}_r denote the global and regional loss terms, respectively. Here, $\{x\}$ denotes the ensemble predictions, y the targets, v the variables, t the rollout length, and w_v the variable-specific scalings, taken from [4]. The predictions are divided into global and regional domains $\{x\} = \{x_g\} + \{x_r\}$, with the same split applied to the targets. Note that the regional domain in our case is on a regular cartesian grid. λ_r controls the relative importance of the regional loss.

The global and regional loss terms are, respectively:

$$\begin{aligned} \mathcal{L}_g(\{x\}, y) &= \mathcal{L}_{\text{point}}(\{x\}, y), \\ \mathcal{L}_r(\{x\}, y) &= \mathcal{L}_{\text{point}}(\{x\}, y) + \lambda_f \mathcal{L}_{\text{freq}}(\{x\}, y), \end{aligned} \quad (1)$$

where the point-wise terms follow the almost-fair CRPS loss introduced by [10], here decomposed into a mean absolute error (MAE) and a variability term:

Table 2: Training configuration and the cost of the different training stages and substages. The cost is given by Training speed \times Iterations \times GPUs. Learning rate here refers to the effective learning rate used in the parameter update.

Stage	A	B1	B2	C1	C2
Rollout	1	1	2	1	2–4
Iterations	150 k	50 k	30 k	10 k	1 k
Learning rate	3.2e-3	1.6e-3	1e-5	6e-4	6e-5
Warm up iterations	1,000	1,000	1,000	1,000	100
Training speed (s/iter)	1	4–5	6–7	7–8	14–25
Training period (years)	43	43	43	2.3	2.3
Batch size	32	16	16	16	16
GPUs per model	2	4	4	4	4
GPUs	128	128	128	128	128
Total GPU-hours	5,500	7,000	7,000	2,700	2,100

$$\mathcal{L}_{\text{point}}(\{x\}, y) = \sum_p w_p \left[\frac{1}{M} \sum_{i=1}^M |x_i - y| - \frac{1 - \varepsilon}{2M(M-1)} \sum_{i=1}^M \sum_{j=1}^M |x_i - x_j| \right]. \quad (2)$$

Here, p denotes a spatial node (latitude/longitude) and w_p the corresponding node weight. M is the ensemble size, and ε determines the degree of CRPS “fairness”: $\varepsilon = 0$ corresponds to a fully fair CRPS, while $\varepsilon = 1/M$ yields the conventional CRPS. Values close to zero produce an almost-fair loss.

For the spectral loss term, $\mathcal{L}_{\text{freq}}$, we compute the two-dimensional fast Fourier transform (FFT) of each field for both the target and all ensemble members, and then evaluate the fields with the almost-fair CRPS loss:

$$\mathcal{L}_{\text{freq}}(\{x\}, y) = \mathcal{L}_{\text{point}}(\{\text{FFT}(x)\}, \text{FFT}(y)), \quad (3)$$

where $\text{FFT}(x)$ denotes the low-pass filtered Fourier coefficients of field x . The fields are reshaped to rectangular grids before applying the FFT. The spectral term is weighted with a factor λ_f relative to the point-wise term. We perform no frequency weighting, i.e., $w_p = 1$ for the spectral term. Frequencies beyond the Nyquist limit, $k < 2\pi/(2 \times 2.5 \text{ km})$, are removed using a low-pass filter.

Although the loss function contains a significant number of terms, we have not noticed a notable increase in the computation time due to these extra terms, as the time is dominated by the rest of the model.

2.3 Training procedure

We follow a stage-wise training procedure with transfer learning between the different stages, as in [20]. An overview of the stages can be seen in Table 1. In stage A, we pre-train a global model on ERA5 upsampled to an O96 grid ($\sim 100 \text{ km}$ horizontal resolution). Pre-training on coarse resolution saves computational resources and run time.

In stage B, we further train the model using ERA5 on its native N320 grid ($\sim 31 \text{ km}$ resolution, stage B1). This stage is important for the model to learn general weather patterns, necessary since the length of the regional dataset is limited. We proceed with rollout training to learn the multi-step properties, as in [10]. In stage B2, we fine-tune the model on 12-hour rollout with a smaller learning rate.

Stage C is where we introduce the stretched grid, using the Integrated Forecast System (IFS) analysis globally, interpolated to the N320 grid, and the MEPS analysis over the Nordic domain. In stage C1, we train with regional weighting $\lambda_r = 1.0$ (that is, the regional domain is not scaled differently from the global domain) and spectral loss weighting $\lambda_f = 0.1$. We perform 1,000 iterations at each of 12-hour, 18-hour and 24-hour rollout in stage C2. The training configuration of all substages is presented in Table 2.

We keep an ensemble size $M = 2$ and CRPS “fairness” $\varepsilon = 0.05/M = 0.025$ for all runs. The AdamW optimizer [27] is used with the default hyperparameters from that paper. A cosine loss scheduler is applied, going from the starting learning rate to zero during the training. We also apply a warm-up period, where the learning rate increases linearly for the first iterations until we reach the starting learning rate, with 1,000 warm-up steps for stages A, B1, B2 and C1 and 100 warm-up steps for stage C2.

2.4 Computational details

The experiments were carried out on 32 compute nodes on the Leonardo supercomputer. Each node consists of 4 NVIDIA A100 graphical processing units (GPUs), each with 64 GB GPU memory. The Anemoi framework [4, 20, 28], implemented in Pytorch [29], is used to con-

Table 3: List of variables used as input and output in the model. Pressure fields are available on 50 hPa, 100 hPa, 150 hPa, 200 hPa, 250 hPa, 300 hPa, 400 hPa, 500 hPa, 700 hPa, 800 hPa, 850 hPa, 925 hPa, 1000 hPa levels. Forcing fields are input fields only.

Pressure level fields	Single level fields	Forcing fields
Geopotential height	Skin/sea-surface temperature	Solar insolation
Temperature	2 m temperature	Sine of Julian day
Specific humidity	2 m dew point temperature	Sine of latitude
Wind speed u component	10 m wind speed u component	Sine of local time
Wind speed v component	10 m wind speed v component	Sine of longitude
Wind speed w component	Mean sea level pressure	Cosine of Julian day
	Surface air pressure	Cosine of longitude
	Total column integrated water	Cosine of latitude
	6-hour accumulated precipitation*†	Cosine of local time
	Low cloud coverage‡	Land sea mask
	Medium cloud coverage‡	Surface geopotential height
	High cloud coverage‡	
	Total cloud coverage‡	
	Surface solar radiation downwards*	
	Surface thermal radiation downwards*	

* diagnostic variable

† rectified linear unit (ReLU) bounding applied

‡ hard tanh bounding applied with range 0 to 1

struct the model and graphs and train the model. The Anemoi framework supports three ways to run training in parallel: Run batches in parallel (data-parallel), run ensemble members in parallel and shard the model across multiple GPUs (model parallel). Model sharding is done both across the grids, processor mesh and attention heads, and is vital to fit the model in GPU memory on a single node.

In our experiments we consequently shard the model across N GPUs to minimize the communication overhead, and run batches and members in parallel across nodes. The number of GPUs requested during training is therefore $N_{\text{GPUs}} = M \times B \times N$, with M and B as the number of members and the batch size, respectively. In stage A the model is only sharded across $N = 2$ GPUs, meaning that we can afford a larger batch size $B = 32$, which effectively reduces the training wall-clock time. For the other stages, the model is sharded across $N = 4$ GPUs for memory reasons, and we use $B = 16$. The total cost of training the final model is around 25,000 GPU hours.

We have also trained a model without a spectral term (setting $\lambda_f = 0$) as a reference for visual properties. For that model, we start from the pre-trained model from stage B, and run stage C1 only. This model is referred to as *Bris CRPS*.

3 Datasets

Our stretched-grid model can be flexible in terms of spatial resolution, and we utilize this property by training it on datasets of various resolutions. The temporal resolution is fixed at 6 hours. For pre-training (stages A and B), we

use the ERA5 reanalysis [25] with training period 1979-01-01T00Z to 2021-12-31T18Z (43 years) and keep the year 2022 for validation. In total, 97 variables are input to the model and 87 variables are predicted, where 3 are diagnostic. We include 15 single level variables and 6 variables at 12 pressure levels. We refer to Table 3 for an overview of the variables. We use the variable weights from [4], and $w_p = 1$ for variables that were not included in that work.

Our stretched-grid formulation (stage C) requires both a global and a regional dataset, where the variables are consistent with the pre-training. Here we use the analysis of MEPS over the Nordic domain and Integrated Forecast System (IFS) regridded to the ERA5 grid elsewhere. 6-h precipitation are retrieved from the first 6 hours of t control run forecasts. The training period here is from 2020-02-05T00Z to 2022-05-31T18Z (2.3 years), and we keep 2022-06-01T00Z to 2023-06-01T00Z for validation. We trim the boundaries of MEPS 125 km in all directions to avoid the model learning from data in the relaxation zone of the NWP analyses.

All datasets used in training and for inference initialization correspond to the control analysis, and are thus deterministic. We apply max normalization for surface geopotential, no normalization on the cloud coverage variables and forcings, and standard normalization on the remaining variables. A ReLU bounding [30] was applied for precipitation to avoid negative values, while a hard tanh bounding [31] was applied for cloud coverage variables to keep the range between 0 and 1.

4 Results and discussion

This section evaluates the quality of the weather forecasts from the perspective of a public weather forecast provider. To achieve this, we focus on surface variables of high relevance to end users, including air temperature at 2m, wind speed at 10m, precipitation (accumulated over 6 hours) and mean sea-level pressure. We divide our verification into single member and probabilistic evaluation.

With the exception of the discrete cosine transform (DCT) results, all forecasts were verified against measurements from 254 synoptic weather stations throughout Norway. Forecasts were interpolated bilinearly to the observation points from the 4 nearest grid points in the model. As temperature is strongly related to altitude, we adjusted the interpolated temperatures by assuming a constant lapse rate of $6.5^{\circ}\text{C}/\text{km}$. This was applied to the altitude mismatch between the bilinearly interpolated altitude field and the station altitude, as has been done in [20].

4.1 Single member evaluation

In this section, we evaluate the characteristics of the forecasted fields from a single ensemble member. We use the MEPS control member and pick a random ensemble member from Bris and AIFS-CRPS. We also include Bris MSE in this comparison, to highlight the benefits of a probabilistic model.

Fig. 2 compares the 6-hour accumulated precipitation fields for an event initialized on 2022-06-01T00Z with a lead time of 18h, for MEPS, Bris MSE, Bris CRPS, and Bris CRPS-FFT. MEPS tends to produce banded precipitation structures that reflect the dynamics of rain showers. It can also represent sharp features such as localized heavy precipitation. We treat the MEPS field as the reference here. In contrast, Bris MSE smoothens out unpredictable events, such as heavy rainfall, which is evident from the overly smooth field structures. This smoothing results in a loss of detail, making it difficult to distinguish between sparse, localized showers and widespread light rain. Bris CRPS, on the other hand, demonstrates an improved ability to capture localized events but introduces substantial small-scale noise, which reduces the spatial coherence of such events.

Bris CRPS-FFT strikes a better balance, by preserving sharp features while preserving more of the spatial correlation. Although some residual small-scale noise clearly is still present, it is less pronounced than in Bris CRPS. Fig. 3 provides a zoomed-in view of the rain showers over southern Norway, clearly highlighting the differences in precipitation forecasts among the models.

Fig. 4 shows a quantile-quantile (QQ) plot for 6-hour accumulated precipitation and 10m wind speed, where sorted observations are plotted against sorted forecasts to assess the similarity between their distributions. While Bris CRPS-FFT underestimates the frequency of larger precipitation events, it performs better than Bris MSE,

highlighting the added value of training Bris with a probabilistic approach. AIFS-CRPS also underestimates precipitation due to the relatively coarse resolution. MEPS overestimates precipitation, but is closer to the ideal line than Bris CRPS-FFT.

All models in this comparison underestimate wind speed, a bias that can partially be attributed to the verification of gridded model outputs against point measurements. Bilinear interpolation between grid points smooths out local extremes, such as high wind speeds, resulting in systematically lower interpolated values compared to actual point observations. However, the relative differences between the models is interesting. A comparison between AIFS-CRPS and Bris CRPS-FFT highlights the potential advantage of higher spatial resolution, with Bris CRPS-FFT exhibiting a more realistic distribution. Furthermore, Bris CRPS-FFT shows notable improvement over Bris MSE in predicting higher wind speeds. Surprisingly, Bris CRPS-FFT is closer to the ideal line than MEPS, which is unexpected and not entirely desirable. The goal for Bris CRPS-FFT is to replicate the distribution of the target, represented by the MEPS analysis. The reason why Bris CRPS-FFT produces higher values than MEPS remains unclear and warrants further investigation.

To evaluate the ability of Bris CRPS-FFT to represent events across different spatial scales, we analyze the power spectra of the forecasts. The power spectrum is computed using the discrete cosine transform (DCT) [32] instead of the standard fast Fourier transform (FFT) to mitigate boundary-related artifacts. Consistent with the approach used in the spectral loss calculation, frequencies above the Nyquist limit are filtered out.

Figure 5 presents the DCT power spectra for wind speed at lead times of +6 h and +60 h for Bris CRPS-FFT, Bris CRPS, Bris MSE, and MEPS (upper row). To highlight the differences between the models, the logarithmic difference with respect to MEPS is also shown (lower row), with MEPS treated as the reference.

The analysis indicates that the power spectra for Bris CRPS-FFT closely align with those of MEPS for wavelengths longer than 10 km. However, excess energy is evident at the smallest scales, reflecting the high-frequency noise observed in Figs. 2 and 3. In contrast, Bris MSE exhibits a significant lack of energy for wavelengths shorter than 300 km, while Bris CRPS shows excessive noise at wavelengths below 50 km. Notably, the power spectra remain largely consistent when comparing lead times of +6 h and +60 h.

4.2 Probabilistic evaluation

To evaluate the probabilistic properties of the forecasts, we generate 10 ensemble members for the entire verification period (2022-06-01T00Z to 2023-05-31T18Z) and compare with MEPS, which runs operationally with 30 members. As MEPS only provides forecasts up to 60 hours into the future, we focus the comparison on short-

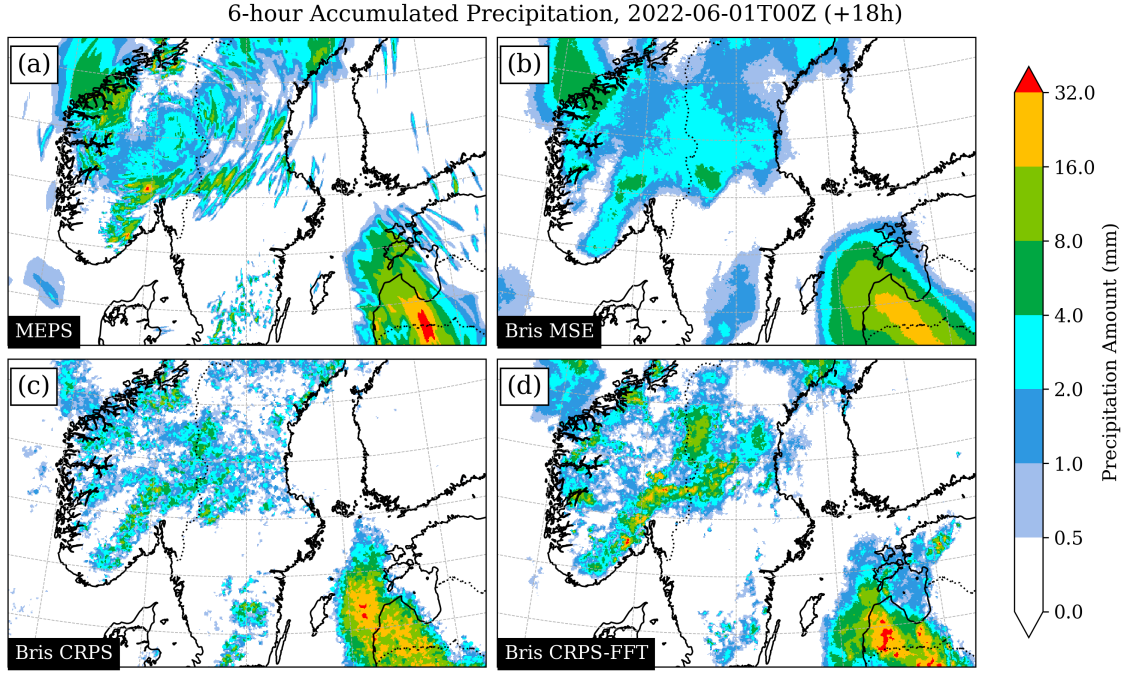


Figure 2: Precipitation fields over parts of the Nordics at 2.5 km horizontal resolution. Each panel represent different forecasting models: (a) The control member of the NWP modelling system MEPS. (b) Bris MSE, as described in [20]. (c) Bris CRPS, trained with point-wise Continuous Ranked Probability Score (CRPS) only. (d) Bris CRPS-FFT trained with point-wise and spectral CRPS. Forecasts are initialized at 2022-06-01T00Z and have a lead time of 18 hours.

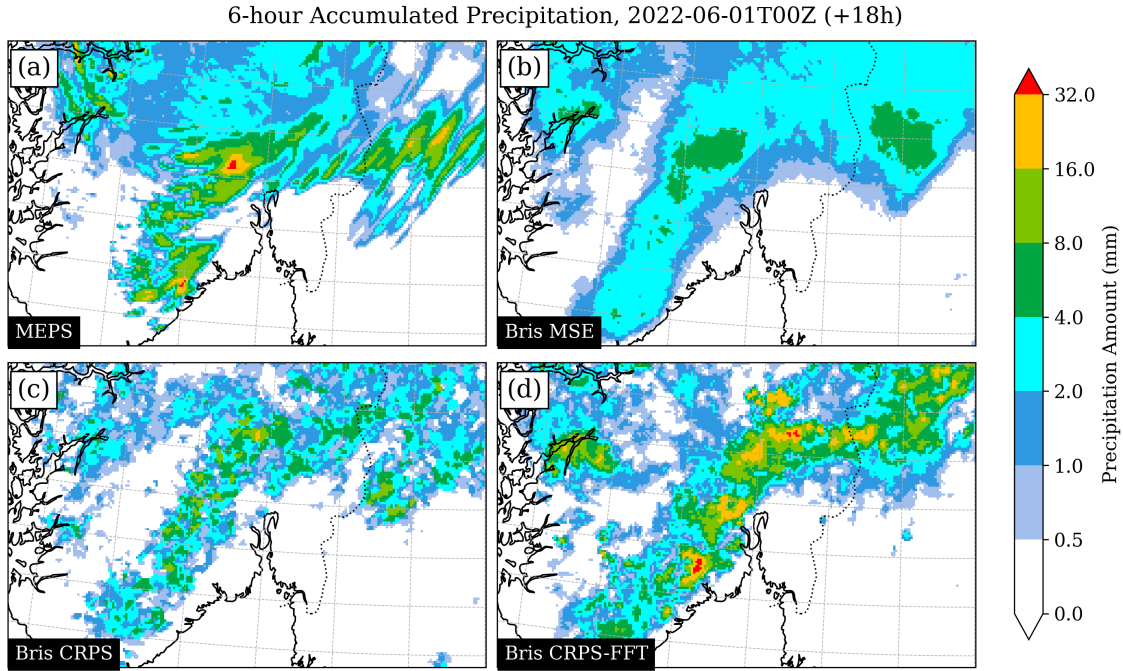


Figure 3: Same as Fig. 2, but zoomed in over southern Norway.

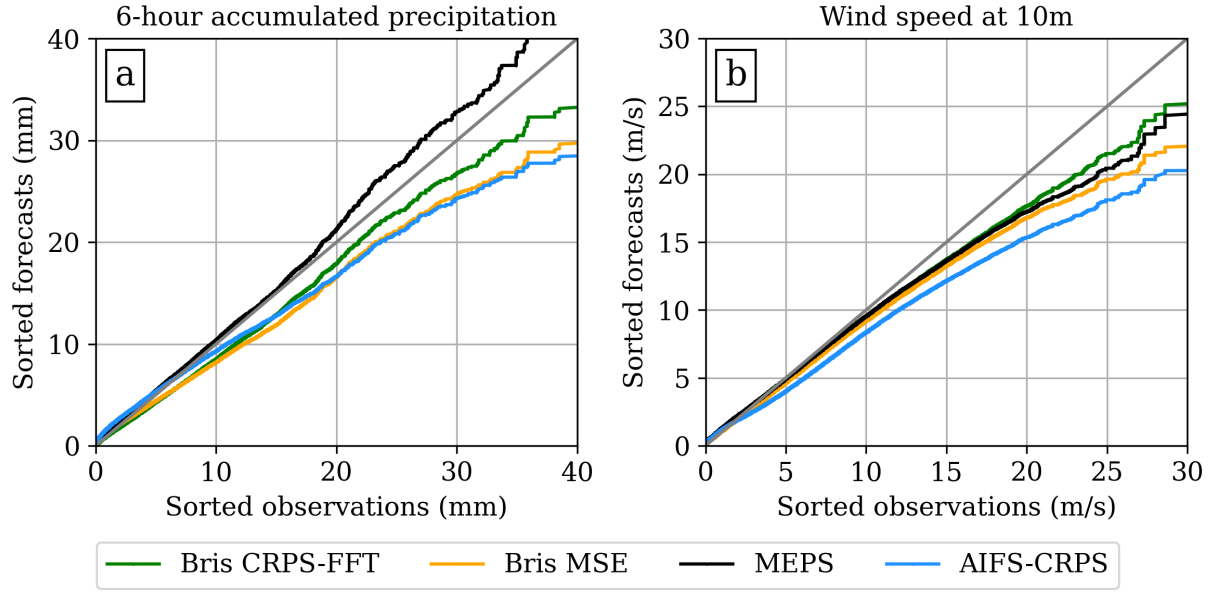


Figure 4: Quantile-quantile (QQ) plot aggregated over lead times 24h–60h. Forecasts are plotted as a function of observations, with the ideal case (gray line) being when the forecasts equal the observations. (a) is precipitation and (b) is wind speed.

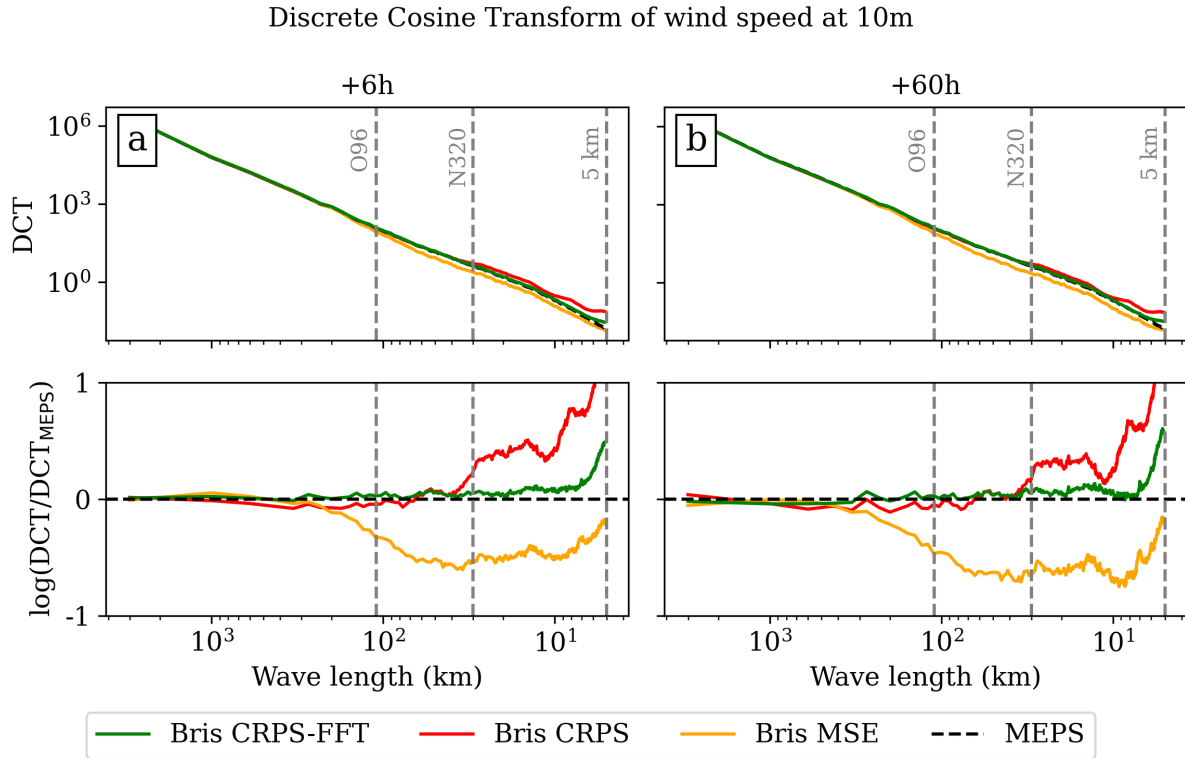


Figure 5: Discrete cosine transform (DCT) of 10m wind speed as a function of wave length for lead times +6h, and +60h (upper row), and the corresponding logarithmic difference with respect to MEPS (lower row). The x-axis is flipped such that the wave lengths increase to the left. The power spectra are averaged from 2022-06-01T00Z to 2022-07-01T00Z.

range forecasts. Additionally, we compare the model to 10 ensemble members generated by AIFS-CRPS [10] at a coarser resolution of 31 km, in order to assess the added value of using a higher-resolution DDM. It is important to note that, in this setup, AIFS-CRPS is initialized with the control analysis from IFS, rather than the perturbed analyses from all ensemble members, in order to make it more comparable to Bris.

To evaluate the probabilistic forecast skill, the CRPS metric is a natural starting point, as it is a proper scoring rule and the model is trained to optimize this variable. For this analysis, we use fair CRPS [33] (fCRPS), using Eq. 2 with $\varepsilon = 0$. Fig. 6 shows the fCRPS as a function of lead time, based on forecasts at the locations of 254 synoptic weather stations in Norway.

For temperature, we observe a clear improvement at all lead times compared to MEPS. This is likely due in part to the MEPS model’s inability to retain analysis increments forward in time. That is, MEPS temperature analyses are significantly more accurate than its forecasts, as discussed in [20].

For wind speed, Bris CRPS-FFT performs comparably to MEPS, with both high-resolution models outperforming AIFS-CRPS. The lower performance of AIFS-CRPS is expected, given its coarse spatial resolution, making it challenging to accurately represent 10 m wind speeds in mountainous regions.

For precipitation, Bris CRPS-FFT performs slightly worse than MEPS at lead times up to 12 hours, but achieves similar performance at longer lead times. The difference for short lead times is likely due to MEPS being initialized from an ensemble of perturbed initial states, capturing initial state uncertainty, whereas Bris is initialized solely from the analysis of the MEPS control run. This highlights a potential area for improvement for Bris CRPS-FFT.

For mean sea-level pressure, Bris CRPS-FFT and MEPS perform similarly. Notably, this is the only one of the variables presented here, where AIFS-CRPS outperforms the other models.

We evaluate the ensemble spread-skill relationship by plotting root mean square error (RMSE) of the ensemble mean and spread in the same plots (Fig. 7). The ensemble spread is calculated from the standard deviation across ensemble members. For an ideal spread-skill ratio, the RMSE (solid lines) and spread (dashed lines) should overlap completely. However, since we verify against observations, the RMSE of the model is expected to be higher than the spread. This is because model grid points represents a larger spatial scale than the observations, and the observations are therefore not representative of the whole grid cell.

For all variables other than wind speed, Bris CRPS-FFT has less spread than MEPS. A likely explanation of this is that Bris CRPS-FFT has been trained against the control analysis of MEPS, which in reality is uncertain. The ensemble therefore will only aims to represent the uncertain

evolution of the control analysis. This also suggest a potential benefit of initializing Bris CRPS-FFT on an ensemble of analyses that can capture initial condition uncertainty. Despite having too little spread, the RMSE of the ensemble mean for Bris CRPS-FFT is in general better than for MEPS, except for wind speed.

In Fig. 8, we have plotted the Brier skill score (BSS) [34] as a function of thresholds for precipitation and wind speed. For precipitation, Bris CRPS-FFT and MEPS performs similar, where MEPS is slightly better for small precipitation amounts and Bris CRPS-FFT is slightly better at high precipitation amounts. For wind speed, Bris CRPS-FFT performs worse for all thresholds. Since MEPS and CRPS-FFT perform similarly for fair-CRPS on wind speed, as seen above, this difference might be partly explained by the difference in ensemble size.

5 Conclusion

In this article, we have presented Bris CRPS-FFT, a high-resolution probabilistic DDM trained on point-wise and spectral CRPS. The model provides forecasts with similar forecast skill as the state-of-the-art local area NWP ensemble prediction system MEPS. For 2m temperature, Bris CRPS-FFT has up to 15% lower fCRPS for some lead times compared to MEPS.

We have shown that the spatial characteristics of single ensemble members are closer to that of NWP models than fields from an MSE-based DDM. Incorporating terms into the loss function that assess the model’s ability to represent different spatial scales was essential to produce coherent fields.

The current model operates at 6-hour temporal resolution, which is too coarse for many applications. In a future work we will increase the temporal resolution to hourly forecasts, better matching our high spatial resolution. Additionally, although spatial coherence of Bris CRPS-FFT is significantly better than Bris CRPS, further modifications to the loss function or the model architecture may be necessary to further improve the spatial structures in the fields. In particular, the energy spectrum of the fields indicate too much energy at the very finest scales.

Issuing timely and reliable extreme-weather warnings is a core responsibility of national meteorological and hydrological services (NMHSes). Yet forecasting high-impact events remains challenging because such phenomena are short-lived, spatially localized, and sensitive to initial-condition uncertainty. High-resolution probabilistic guidance is therefore essential for meeting operational warning requirements. In this context, DDMs offer a promising pathway for next-generation extreme-weather prediction owing to their fast forecasting speed and capacity for ensemble generation. Furthermore, the stretched-grid design of Bris CRPS-FFT enables efficient operational deployment; the system has been running operationally at MET Norway four times a day since October 2025.

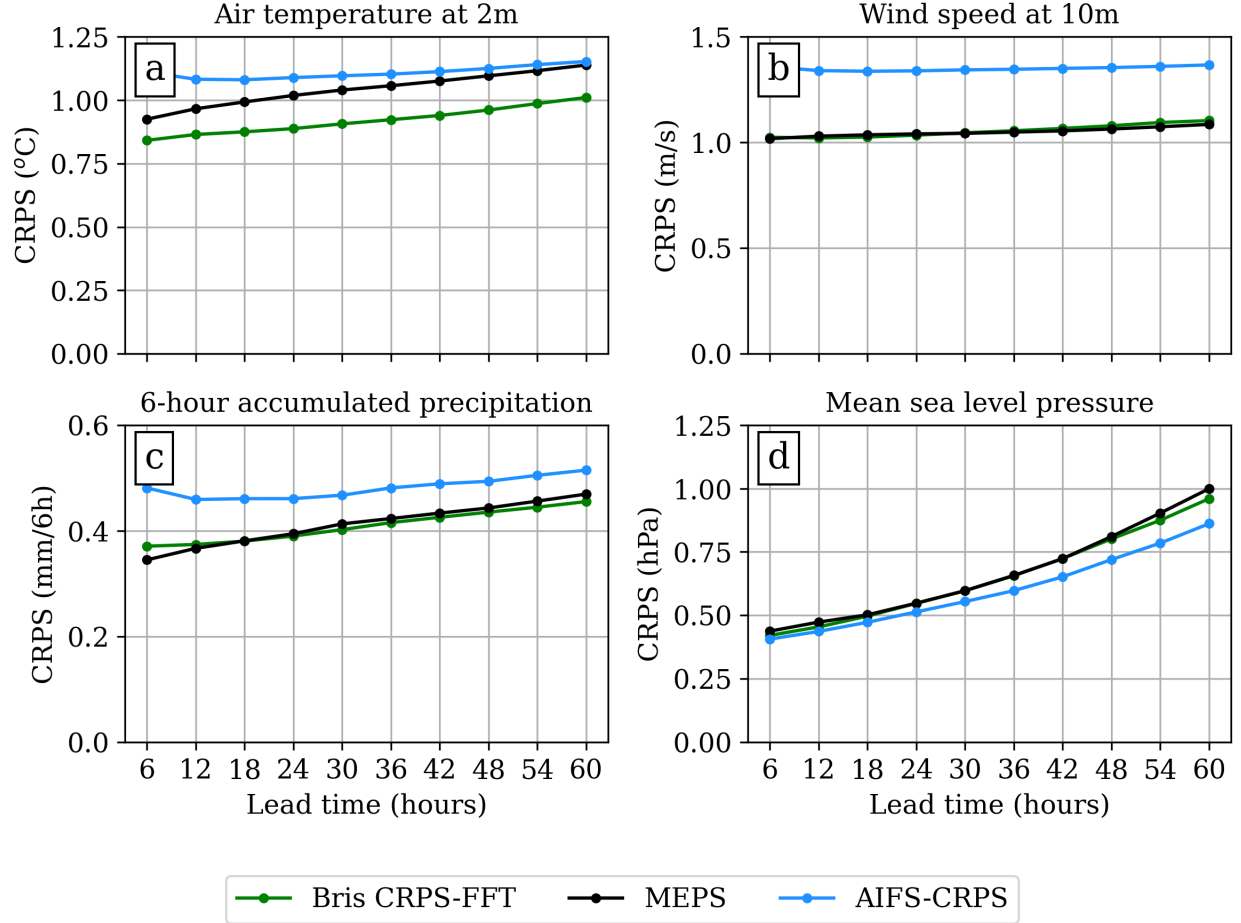


Figure 6: Fair Continuous Ranked Probability Score (CRPS) plotted as a function of lead time for 2m temperature (a), 10m wind speed (b), 6h precipitation (c) and mean sea-level pressure (d). Lower score is better.

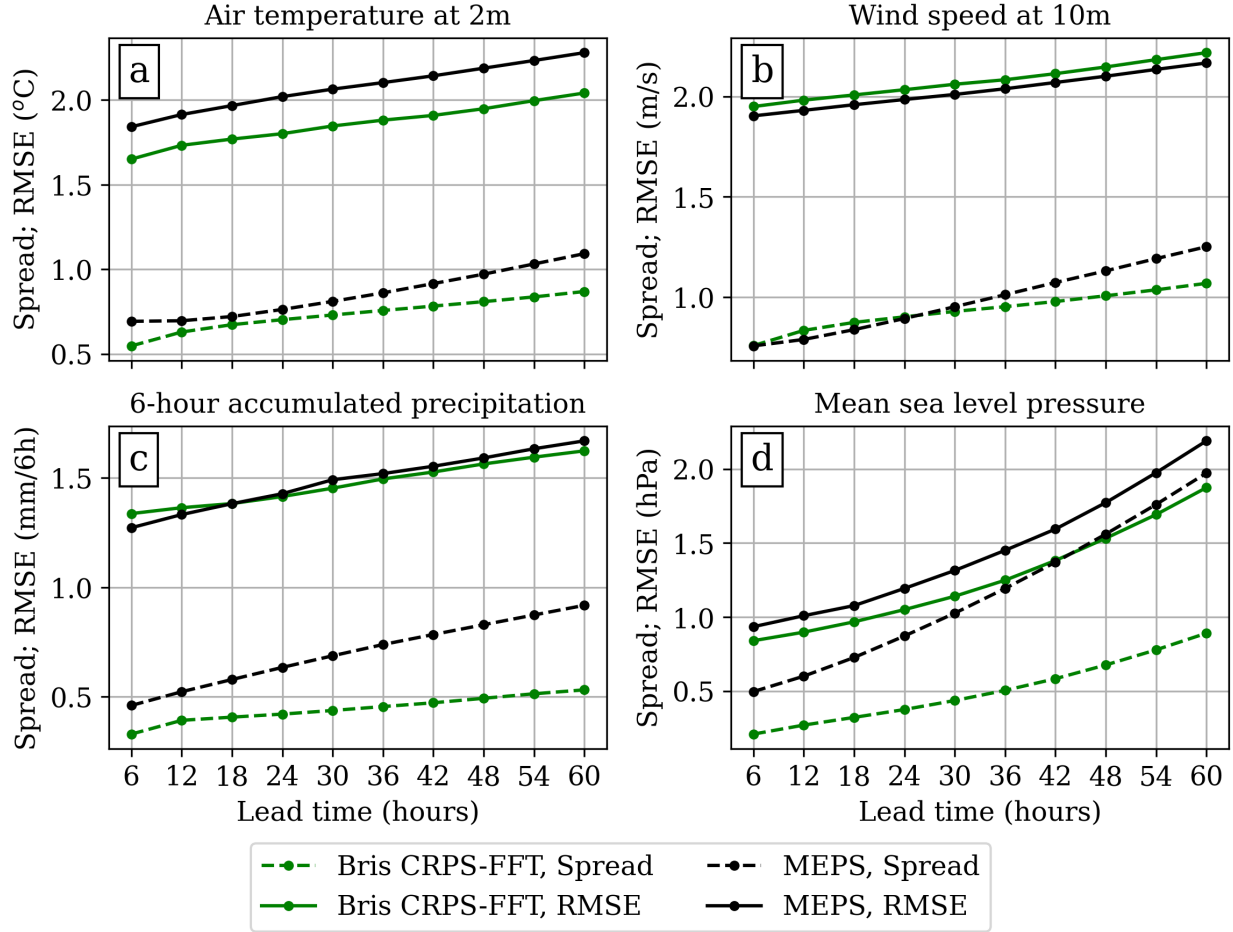


Figure 7: Spread (dashed lines) and root mean square error (RMSE) of the ensemble mean (solid lines) as a function of lead times for 2m temperature (a), 10m wind speed (b), 6h precipitation (c) and mean sea-level pressure (d). Overlapping spread and RMSE curves gives a perfect spread-skill ratio.

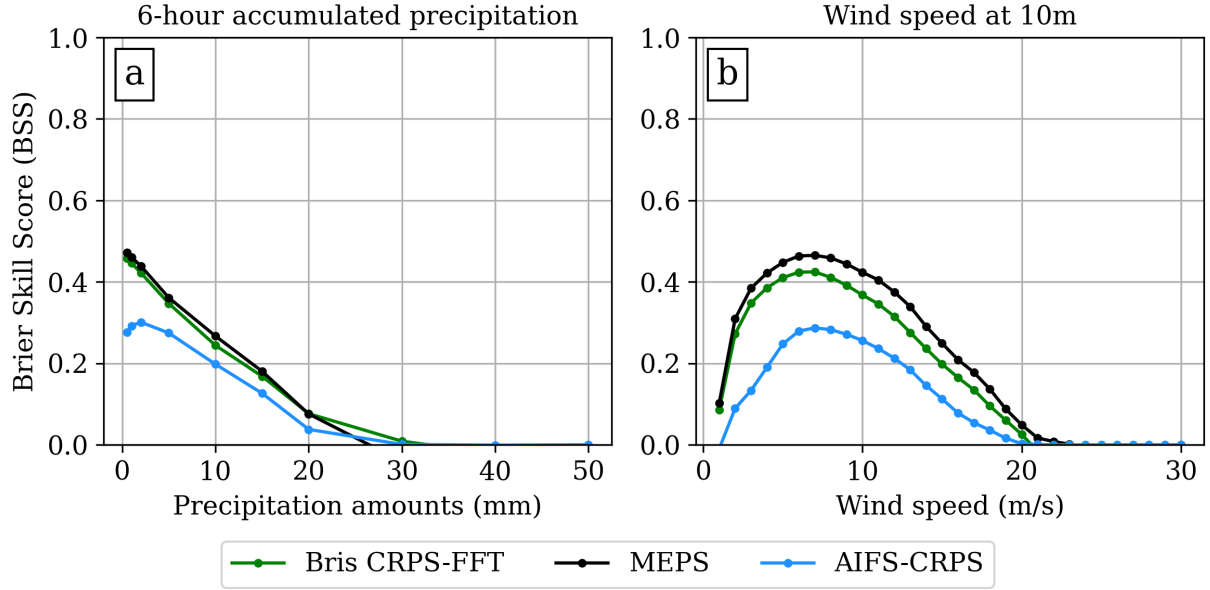


Figure 8: Brier skill score (BSS) as a function of thresholds for 6h precipitation (a) and 10m wind speed (b). Higher score is better.

Acknowledgments

This work was funded by the Horizon Europe project WeatherGenerator (grant agreement 101187947). Computing and storage resources were provided by EuroHPC through the regular access call EHPC-REG-2024R02-079. Thanks to Svante Henriksson, Bastien Francois and Boris Bonev for fruitful discussions about how to set up the loss objective.

References

- [1] J. Pathak, S. Subramanian, P. Harrington, S. Raja, A. Chattopadhyay, M. Mardani, T. Kurth, D. Hall, Z. Li, K. Azizzadenesheli, P. Hassanzadeh, K. Kashinath, and A. Anandkumar, “FourCastNet: A Global Data-driven High-resolution Weather Model using Adaptive Fourier Neural Operators,” Feb. 2022. arXiv:2202.11214.
- [2] K. Bi, L. Xie, H. Zhang, X. Chen, X. Gu, and Q. Tian, “Accurate medium-range global weather forecasting with 3D neural networks,” *Nature*, vol. 619, pp. 533–538, July 2023. Publisher: Nature Publishing Group.
- [3] L. Chen, X. Zhong, H. Li, J. Wu, B. Lu, D. Chen, S.-P. Xie, L. Wu, Q. Chao, C. Lin, Z. Hu, and Y. Qi, “A machine learning model that outperforms conventional global subseasonal forecast models,” *Nature Communications*, vol. 15, p. 6425, July 2024. Publisher: Nature Publishing Group.
- [4] S. Lang, M. Alexe, M. Chantry, J. Damsch, F. Pinault, B. Raoult, M. C. A. Clare, C. Lessig, M. Maier-Gerber, L. Magnusson, Z. B. Bouallègue, A. P. Nemesio, P. D. Dueben, A. Brown, F. Pappenberger, and F. Rabier, “AIFS - ECMWF’s data-driven forecasting system,” June 2024. arXiv:2406.01465 [physics].
- [5] E. E. Ebert and J. L. McBride, “Verification of precipitation in weather systems: determination of systematic errors,” *Journal of Hydrology*, vol. 239, pp. 179–202, Dec. 2000.
- [6] C. Zingerle and P. Nurmi, “Monitoring and verifying cloud forecasts originating from operational numerical models,” *Meteorological Applications*, vol. 15, no. 3, pp. 325–330, 2008. eprint: <https://rmets.onlinelibrary.wiley.com/doi/pdf/10.1002/met.73>.
- [7] C. Subich, S. Z. Husain, L. Separovic, and J. Yang, “Fixing the Double Penalty in Data-Driven Weather Forecasting Through a Modified Spherical Harmonic Loss Function,” Jan. 2025. arXiv:2501.19374 [cs].
- [8] W. Xu, K. Chen, T. Han, H. Chen, W. Ouyang, and L. Bai, “ExtremeCast: Boosting Extreme Value Prediction for Global Weather Forecast,” May 2024. arXiv:2402.01295 [cs].
- [9] D. Kochkov, J. Yuval, I. Langmore, P. Norgaard, J. Smith, G. Mooers, M. Klöwer, J. Lottes, S. Rasp, P. Düben, S. Hatfield, P. Battaglia, A. Sanchez-Gonzalez, M. Willson, M. P. Brenner, and S. Hoyer, “Neural general circulation models for weather and climate,” *Nature*, vol. 632, pp. 1060–1066, Aug. 2024. Publisher: Nature Publishing Group.
- [10] S. Lang, M. Alexe, M. C. A. Clare, C. Roberts, R. Adewoyin, Z. B. Bouallègue, M. Chantry, J. Damsch, P. D. Dueben, S. Hahner, P. Maciel, A. Prieto-Nemesio, C. O’Brien, F. Pinault, J. Polster, B. Raoult,

- S. Tietsche, and M. Leutbecher, “AIFS-CRPS: Ensemble forecasting using a model trained with a loss function based on the Continuous Ranked Probability Score,” Dec. 2024. arXiv:2412.15832 [physics].
- [11] F. Alet, I. Price, A. El-Kadi, D. Masters, S. Markou, T. R. Andersson, J. Stott, R. Lam, M. Willson, A. Sanchez-Gonzalez, and P. Battaglia, “Skillful joint probabilistic weather forecasting from marginals,” June 2025. arXiv:2506.10772 [cs].
- [12] B. Bonev, T. Kurth, A. Mahesh, M. Bisson, J. Kossafi, K. Kashinath, A. Anandkumar, W. D. Collins, M. S. Pritchard, and A. Keller, “FourCastNet 3: A geometric approach to probabilistic machine-learning weather forecasting at scale,” July 2025. arXiv:2507.12144 [cs].
- [13] M. Schillinger, M. Samarin, X. Shen, R. Knutti, and N. Meinshausen, “EnScale: Temporally-consistent multivariate generative downscaling via proper scoring rules,” Sept. 2025. arXiv:2509.26258 [physics].
- [14] T. Gneiting and A. E. Raftery, “Strictly Proper Scoring Rules, Prediction, and Estimation,” *Journal of the American Statistical Association*, vol. 102, pp. 359–378, Mar. 2007. Publisher: ASA Website _eprint: <https://doi.org/10.1198/016214506000001437>.
- [15] I. Price, A. Sanchez-Gonzalez, F. Alet, T. R. Andersson, A. El-Kadi, D. Masters, T. Ewalds, J. Stott, S. Mohamed, P. Battaglia, R. Lam, and M. Willson, “Probabilistic weather forecasting with machine learning,” *Nature*, vol. 637, pp. 84–90, Jan. 2025. Publisher: Nature Publishing Group.
- [16] M. Alexe, S. Lang, M. Clare, M. Leutbecher, C. Roberts, L. Magnusson, M. Chantry, R. Adeyoyin, A. Prieto-Nemesio, J. Dramsch, F. Pinault, and B. Raoult, “Data-driven ensemble forecasting with the AIFS,” Oct. 2024.
- [17] E. Larsson, J. Oskarsson, T. Landelius, and F. Lindsten, “Diffusion-LAM: Probabilistic Limited Area Weather Forecasting with Diffusion,” Feb. 2025. arXiv:2502.07532 [cs].
- [18] J. Oskarsson, T. Landelius, M. P. Deisenroth, and F. Lindsten, “Probabilistic Weather Forecasting with Hierarchical Graph Neural Networks,” June 2024. arXiv:2406.04759 [cs, stat].
- [19] S. Adamov, J. Oskarsson, L. Denby, T. Landelius, K. Hintz, S. Christiansen, I. Schicker, C. Osuna, F. Lindsten, O. Fuhrer, and S. Schemm, “Building Machine Learning Limited Area Models: Kilometer-Scale Weather Forecasting in Realistic Settings,” Apr. 2025. arXiv:2504.09340 [physics].
- [20] T. N. Nipen, H. H. Haugen, M. S. Ingstad, E. M. Nordhagen, A. F. S. Salihi, P. Tedesco, I. A. Seierstad, J. Kristiansen, S. Lang, M. Alexe, J. Dramsch, B. Raoult, G. Mertes, and M. Chantry, “Regional data-driven weather modeling with a global stretched-grid,” *Artificial Intelligence for the Earth Systems*, vol. -1, Nov. 2025. Publisher: American Meteorological Society Section: Artificial Intelligence for the Earth Systems.
- [21] J. Baño-Medina, A. Sengupta, D. Steinhoff, P. Mulrooney, T. Nipen, M. Santa-Cruz, Y. Nie, and L. D. Monache, “A Regional High Resolution AI Weather Model for the Prediction of Atmospheric Rivers and Extreme Precipitation,” July 2025. ISSN: 2693-5015.
- [22] R. Keisler, “Forecasting Global Weather with Graph Neural Networks,” Feb. 2022. arXiv:2202.07575 [physics].
- [23] I.-L. Frogner, A. T. Singleton, M. \. K{\o}ltzow, and U. Andrae, “Convection-permitting ensembles: Challenges related to their design and use,” *Quarterly Journal of the Royal Meteorological Society*, vol. 145, no. S1, pp. 90–106, 2019. _eprint: <https://onlinelibrary.wiley.com/doi/pdf/10.1002/qj.3525>.
- [24] M. Müller, M. Homleid, K.-I. Ivarsson, M. A. \. K{\o}ltzow, M. Lindsog, K. H. Midtbø, U. Andrae, T. Aspelien, L. Berggren, D. Bjørge, P. Dahlgren, J. Kristiansen, R. Randriamampianina, M. Ridal, and O. Vignes, “AROME-MetCoOp: A Nordic Convective-Scale Operational Weather Prediction Model,” *Weather and Forecasting*, vol. 32, pp. 609–627, Apr. 2017.
- [25] H. Hersbach, B. Bell, P. Berrisford, S. Hirahara, A. Horányi, J. Muñoz-Sabater, J. Nicolas, C. Peubey, R. Radu, D. Schepers, A. Simmons, C. Soci, S. Abdalla, X. Abellan, G. Balsamo, P. Bechtold, G. Biavati, J. Bidlot, M. Bonavita, G. De Chiara, P. Dahlgren, D. Dee, M. Diamantakis, R. Dragani, J. Flemming, R. Forbes, M. Fuentes, A. Geer, L. Haimberger, S. Healy, R. J. Hogan, E. Hólm, M. Janisková, S. Keeley, P. Laloyaux, P. Lopez, C. Lupu, G. Radnoti, P. de Rosnay, I. Rozum, F. Vamborg, S. Villaume, and J.-N. Thépaut, “The ERA5 global reanalysis,” *Quarterly Journal of the Royal Meteorological Society*, vol. 146, no. 730, pp. 1999–2049, 2020.
- [26] S. Lang, M. Leutbecher, and P. Maciel, “A multi-scale loss formulation for learning a probabilistic model with proper score optimisation,” June 2025. arXiv:2506.10868 [physics].
- [27] I. Loshchilov and F. Hutter, “Decoupled Weight Decay Regularization,” Jan. 2019. arXiv:1711.05101 [cs, math].
- [28] J. S. Wijnands, M. V. Ginderachter, B. François, S. Buurman, P. Termonia, and D. V. d. Bleeken, “A comparison of stretched-grid and limited-area modelling for data-driven regional weather forecasting,” July 2025. arXiv:2507.18378 [physics].
- [29] A. Paszke, S. Gross, F. Massa, A. Lerer, J. Bradbury, G. Chanan, T. Killeen, Z. Lin, N. Gimselshein, L. Antiga, A. Desmaison, A. Köpf, E. Yang, Z. DeVito, M. Raison, A. Tejani, S. Chilamkurthy, B. Steiner, L. Fang, J. Bai, and S. Chintala, “PyTorch:

- An Imperative Style, High-Performance Deep Learning Library,” Dec. 2019. arXiv:1912.01703 [cs, stat].
- [30] V. Nair and G. E. Hinton, “Rectified linear units improve restricted boltzmann machines,” in *Proceedings of the 27th International Conference on International Conference on Machine Learning, ICML’10*, (Madison, WI, USA), pp. 807–814, Omnipress, June 2010.
 - [31] X. Glorot, A. Bordes, and Y. Bengio, “Deep Sparse Rectifier Neural Networks,” in *Proceedings of the Fourteenth International Conference on Artificial Intelligence and Statistics*, pp. 315–323, JMLR Workshop and Conference Proceedings, June 2011. ISSN: 1938-7228.
 - [32] J. Makhoul, “A fast cosine transform in one and two dimensions,” *IEEE Transactions on Acoustics, Speech, and Signal Processing*, vol. 28, pp. 27–34, Feb. 1980.
 - [33] C. a. T. Ferro, “Fair scores for ensemble forecasts,” *Quarterly Journal of the Royal Meteorological Society*, vol. 140, no. 683, pp. 1917–1923, 2014. _eprint: <https://rmets.onlinelibrary.wiley.com/doi/pdf/10.1002/qj.2270>.
 - [34] G. W. Brier, “VERIFICATION OF FORECASTS EXPRESSED IN TERMS OF PROBABILITY,” *Monthly Weather Review*, vol. 78, pp. 1–3, Jan. 1950. Publisher: American Meteorological Society Section: Monthly Weather Review.